Multi-Line Acquisition With Minimum Variance Beamforming in Medical Ultrasound Imaging

Adi Rabinovich, Zvi Friedman, and Arie Feuer, *Fellow, IEEE*

***Abstract*—In recent years, multiple-line acquisition (MLA) has been introduced to increase frame rate in cardiac ultrasound medical imaging. However, this method induces block-like artifacts in the image. One approach suggested, synthetic transmit beamforming (STB), involves overlapping transmit beams which are then interpolated to remove the MLA blocking artifacts. Independently, the application of minimum variance (MV) beamforming has been suggested in the context of MLA. We demonstrate here that each approach is only a partial solution and that combining them provides a better result than applying either approach separately. This is demonstrated by using both simulated and real phantom data, as well as cardiac data. We also show that the STB-compensated MV beamfomer outperforms single-line acquisition (SLA) delay-and-sum in terms of lateral resolution.**

I. Introduction

One of the major challenges in ultrasound today is that of increasing the frame rate. It is important for getting high temporal resolution for fast-moving objects such as the heart in traditional 2-D imaging and, more recently, is even more vitally important in 3-D ultrasound imaging. The frame rate depends on the speed of sound in the medium, number of transmit (Tx) lines per frame, and depth of penetration of the scanned field of view (FOV).

A major constraint on the frame rate is the number of transmitting lines covering the FOV. In standard ultrasound imaging there, is a receive (Rx) line created for each Tx line. Together, they give the Tx-Rx or 2-way beam profile, which is the multiplication of the Tx by the Rx beam profiles. This improves SNR by a square factor. Because the beam profiles are the Fourier transforms at the far field (or focal point) of a finite aperture, their profiles have a main lobe and side lobes and are symmetric when the aperture shading is real. This means that the overall Tx-Rx profile also has this symmetric form with a main lobe and side lobes.

Potentially, one can attempt to produce several Rx lines from a wider transmit profile covering the same lateral FOV as several Rx lines. This is called multi-line acquisition (MLA), or parallel receive beamforming (PRB), and was originally proposed in [1] and [2].

Manuscript received July 10, 2013; accepted August 7, 2013.

A. Rabinovich and A. Feuer are with the Department of Electrical Engineering, Technion, Israel Institute of Technology, Haifa, Israel (e-mail: feuer@ee.technion.ac.il).

Z. Friedman is with GE Healthcare, Tel-Aviv, Israel.

DOI http://dx.doi.org/10.1109/TUFFC.2013.2851

There are several inherent problems with this method. One problem is the shifting of the peak location of the Tx-Rx beam profile's main lobe. It happens because the Tx and Rx beam profiles are no longer aligned, hence the Tx-Rx peak will lie between the peaks of the Tx and Rx profiles. This is called warping. Another problem stems from the fact that the Tx-Rx beam profile is no longer symmetric—this is called skewing. A third problem is the gain loss because the energy is not concentrated at the center of the Tx-Rx profile, but rather spread out more; hence, the peak of the Tx-Rx beam profile is lower when using single-line acquisition (SLA) mode. All these effects are described in detail in [3].

However, the strongest effect noticeable when using MLA is the decorrelation of the Rx lines in the transition region between adjacent MLA group lines. It creates a lateral block-like appearance in the image that intensifies as the number of Rx lines per Tx line increases. There is also much loss of lateral resolution in an MLA group region because strong reflectors tend to smear out all over the lateral Tx region. This happens because of the lack of focus in transmit. As the transmission needs to cover a wider area, strong reflectors will appear all over the main lobe of the wide Tx profile and will not be reduced by the side lobes, as in standard SLA.

To compensate for these artifacts, several approaches were proposed in the patent literature, such as sinc apodization on transmit [4], dynamic steering [5], [6], or incoherent interpolation after RF detection [7], [8]. The most prominent approach that utilizes coherent interpolation before beamforming was suggested in [3] and [9]. This approach, called synthetic transmit beamforming (STB), proposes generating the Rx lines by linear interpolation of the delayed-and-summed (DAS) Rx lines generated from adjacent overlapping Tx lines. We will describe the STB method in some detail in the following. In [3], it is shown that the STB does reduce the artifacts of MLA beamforming, especially the block-like appearance, because it highly correlates adjacent Rx lines, even those belonging to different Tx regions. However, it seems to suffer from loss of resolution and contrast because of the interpolations it involves.

Synnevag *et al.* [10] suggest, as one of the benefits in using minimum variance (MV) beamforming, or the Capon beamformer [11], in ultrasound imaging is its application to MLA (or PRB, as they refer to it). They have used 4 Rx lines per transmission to demonstrate that the performance of MV gives good results compared with DAS with

SLA. However, they worked in a simulated environment of Field II [12], which does not emphasize the MLA-induced artifacts in their somewhat simplified examples. In real ultrasound data, and especially in organs such as the heart where strong reflections are present near weak or nonreflecting media, these effects are much more severe. This can be observed in the original STB work [3], in which the block-like artifacts are not seen in a simulated medium with 2MLA (see [3, Fig. 8]), whereas in the subsequent work [13], the results clearly show that real data displays these artifacts (see [13, Fig. 2], for example). Therefore, we feel that there is no evidence in the literature that applying MV in the context of MLA removes the blocking artifacts. On the contrary, to challenge this, we have applied MV beamforming on cardiac data and show that these artifacts still remain.

On the one hand, STB reduces the MLA artifacts at the price of lateral resolution and contrast loss; on the other, MV cannot alleviate the MLA artifacts, but has been shown to improve resolution and contrast (see e.g., [14]–[19]). This realization prompted us to combine the two, and that is what we describe in this paper. To demonstrate the benefits of this combination over the use of each separately, we have used both simulated Field II data and data from real phantoms, as well as data from real cardiac ultrasound imaging. We will show that MV in an MLA setting does not remove the decorrelation block-like artifacts when the Rx lines are generated from a single Tx. We will demonstrate that the STB method does compensate for these artifacts, but when combined with MV can produce better results than STB with fixed apodization alone, and that applying STB with MV can produce better results than applying MV in an MLA setting without STB.

In our next section, we describe briefly the known theory behind the STB approach and MV adaptive beamforming. Section III provides the details of our simulations, the real data set-up, and the wide Tx profile simulation. In Section IV, we present and discuss the results of our experiments, and Section V contains the conclusions drawn from this work.

II. Theory

A. Synthetic Transmit Beamforming (STB)

The full background and motivation for using the STB technique is given in [3]. A brief discussion is provided here for the benefit of the reader. This method creates synthetic transmit beams between the real transmitted beams. Let d, a, and λ be the Tx focal depth, aperture width, and central wavelength, respectively. Then, assuming that the transmit beams sample the scanned FOV at no more than the Nyquist sampling criterion of $d/a\lambda$, by interpolating the sampled data on each aperture element, one can construct data as if received from a synthetic transmit beam in any intermediary direction. The interpolated data can in turn be steered and focused in the direction of the synthetic beam. In this way, we get a (synthetic) transmit beam aligned with the received beam and all of the geometric distortions mentioned earlier are alleviated.

More formally, assume an aperture of M elements transmits B beams transmitted into the FOV of the ultrasound image. For beam $1 < b < B$, the aperture will be focused at point x_b, with a radial depth of $d = ct_0/2$, where c is the speed of sound in the medium and t_0 is the time of flight required to reach depth d. Let $S_m(x_b, n)$ denote the sampled signal received at element m after focusing at point x_b, and $\{S_m(x_b, n)\}_{1<b<B, 1<m<M}$ is the set of collected signals. Using sampling theory and the Nyquist assumption, the signal originating from an intermediate point x_i and received at element m can be found as

$$\tilde{S}_m(x_i, n) = \sum_b h(x_i, b) S_m(x_b, n), \tag{1}$$

where $h(x_i, b)$ is the interpolation filter. Then, the received signal beamformed in the x_i direction can be found by

$$\tilde{S}(x_i, n) = \sum_m \tilde{S}_m(x_i, n - \tau_m(x_i)) \tag{2}$$

$$= \sum_m \sum_b h(x_i, b) S_m(x_b, n - \tau_m(x_i)) \tag{3}$$

$$= \sum_b h(x_i, b) \sum_m S_m(x_b, n - \tau_m(x_i)) \tag{4}$$

$$= \sum_b h(x_i, b) S^b(x_i, n), \tag{5}$$

where $\{\tau_m(x_i)\}_{1<m<M}$ are the time delays corresponding to x_i.

The interchange from (3) to (4) can be done if we assume that the filter $h(x_i, b)$ is linear, shift invariant, and independent of m. It is interesting to observe that the signals $S^b(x_i, n)$ are the results of transmitting in the x_b direction and focusing in the x_i direction in the receive mode. Clearly, for these signals to be non-negligible, there must be a sufficient overlap in the transmit beams because only those overlapping are included in the summation over b. In practice, each x_i is contained in two corresponding values of b and the choice for $h(x_i, b)$ is $[1 - w, w]$ where w is the relative distance (see [3] for more details). This overlap and interpolation is an essential factor in the cure for the blocking artifacts typical in MLA but, as we pointed out earlier, it is also the cause of the loss of resolution and contrast.

We note that in (2), one can add a fixed apodization vector $\mathbf{g} = [g_1, \ldots, g_M]^H$ and the sum over m in (4) will be modified accordingly.

B. Correlation Analysis

Although the geometric distortion artifacts in the transition between MLA groups may be visible in the image,

a quantitative measure is needed to assess its significance, and that of a measurable reduction in the artifacts after applying STB compensation. To assess the decorrelation of adjacent scan lines stemming from MLA in the results section, we have used the quantitative measure introduced in [13]. When the two-way profiles are sampled irregularly, such as without STB-compensated MLA, where two adjacent Rx lines are generated from different Tx beams, the correlation will be low. When the profiles belong to the same Tx beam (same MLA group) it will be higher. When STB compensation is used, the correlation should be approximately the same regardless of the two-way profiles pair examined.

Using the notation

$$\hat{\mathcal{R}}_{ij} = \frac{1}{d}\sum_{r=n-d}^{n-1} y_i[r]y_j^*[r], \tag{6}$$

for the correlation estimate between adjacent Rx scan lines, i and j, with $\hat{}$ denoting estimation, and where $y_i[n]$ is the delayed and beam-summed complex (IQ) signal along scan line i and depth sample n, a correlation coefficient can be defined in the form of

$$C_c = \frac{2\,\mathrm{Real}(\hat{\mathcal{R}}_{ij})}{\hat{\mathcal{R}}_{ii} + \hat{\mathcal{R}}_{jj}}. \tag{7}$$

C_c can be calculated for the whole length of the measured signal (all samples) or a certain subset of length d around the Tx focal region, for example. A C_c plot of adjacent Rx lines can be used to view both the correlation within MLA groups and at the transition regions between MLA groups. In addition, an indicator of fractional correlation coefficient, D_c was defined in [13] as

$$D_c = \frac{\frac{1}{X}\sum_{ij\in W} C_c - \frac{1}{Y}\sum_{ij\in T} C_c}{\frac{1}{X}\sum_{ij\in W} C_c}\cdot 100, \tag{8}$$

where $i \neq j$ are a pair of scan lines, the set W contains all pairs within MLA groups, the set T contains all pairs in the transition regions between MLA groups, and X and Y are the set sizes, accordingly. D_c is 0 when no difference in correlation between MLA groups and transition regions is present, and 100 when there is full correlation within the MLA groups and no correlation between the groups. A negative value appears when there is more correlation on average in the transition regions than within MLA groups.

C. Minimum Variance Beamforming (MV) With STB

The MV beamformer finds the apodization weights at each beamformed point x_i so that the variance of the beamformed signal is minimized while forcing a gain one in the x_i direction. An in-depth description and analysis of MV beamformer can be found in [16] and [17] and references therein. We will briefly describe it here and show how it is modified to be applied with STB.

Consider the beamformed signal as in (2) with apodization

$$\begin{aligned}\tilde{S}(x_i,n) &= \sum_{m-1}^{M} w_m(x_i,n)\tilde{S}_m(x_i, n-\tau_m(x_i)) \\ &= \mathbf{w}^{\mathrm{H}}(x_i,n)\tilde{\mathbf{S}}(x_i,n),\end{aligned} \tag{9}$$

where

$$\mathbf{w}(x_i,n) = [w_1(x_i,n),..., w_M(x_i,n)]^H,$$
$$\tilde{\mathbf{S}}(x_i,n) = \left[\tilde{S}_1^*(x_i,n-\tau_1(x_i)),..., \tilde{S}_M(x_i,n-\tau_M(x_i))\right]^H,$$

$*$ denotes the complex conjugate and H denotes the conjugate transpose (Hermitian). Then, the variance of this signal can be written as

$$E\{|\tilde{S}(x_i,n)|^2\} = \mathbf{w}^{\mathrm{H}}(x_i,n)\mathbf{R}(x_i,n)\mathbf{w}(x_i,n), \tag{10}$$

where $E\{\cdot\}$ denotes the expectation and $\mathbf{R}(x_i,n) = E\{\tilde{\mathbf{S}}(x_i,n)\tilde{\mathbf{S}}(x_i,n)^{\mathrm{H}}\}$ is the spatial covariance matrix. The weight vector minimizing this variance can be found as the solution of

$$\mathbf{w}(x_i,n) = \arg\min_{\mathbf{w}} \mathbf{w}^{\mathrm{H}}\mathbf{R}(x_i,n)\mathbf{w} \text{ such that } \mathbf{w}^{\mathrm{H}}\mathbf{1} = 1, \tag{11}$$

where $\mathbf{1} = [1,\ldots,1]^{\mathrm{T}}$, as the signals across the aperture are pre-steered. The constraint guarantees a gain of 1 in the steered direction. The solution to this problem is known to be

$$\mathbf{w}(x_i,n) = \frac{\mathbf{R}(x_i,n)\mathbf{1}}{\mathbf{1}^{\mathrm{T}}\mathbf{R}(x_i,n)\mathbf{1}}. \tag{12}$$

The MV beamformer adapts to the recorded data, placing nulls in directions where strong interferences appear, large side lobes at low-energy lateral regions, and forcing unit gain at the direction of arrival (DOA), which is the steering angle.

The covariance matrix, $\mathbf{R}(x_i,n)$ is not given and must be estimated from the data. There are several methods to do this for the SLA set up, but the most common one used in [16] is spatial averaging. Spatial averaging is needed because the signals involved are nonstationary, and because signals from different scatterers can be correlated, which may lead to signal cancellation. This may be avoided using sub-array averaging, as described in [20] and [21].

In addition, to achieve speckle statistics similar to DAS, as described in [22], temporal or depth averaging is also needed. The estimate of the covariance matrix with sub-array length L, and $2K+1$ temporal window will be

$$\hat{\mathbf{R}}(x_i,n)=\frac{\sum_{k=-K}^{K}\sum_{\ell=1}^{M-L+1}\overline{\mathbf{S}}_\ell(x_i,n-k)\overline{\mathbf{S}}_\ell^{\mathrm{H}}(x_i,n-k)}{(2K+1)(M-L+1)}, \tag{13}$$

where

$$\overline{\mathbf{S}}_\ell(x_i,n)= [\tilde{S}_\ell^*(x_i,n-\tau_\ell(x_i)),\ldots,\tilde{S}_{\ell+L-1}^*(x_i,n-\tau_{\ell+L-1}(x_i))]^{\mathrm{H}}. \tag{14}$$

We note that the optimization problem is reduced in dimension from M to L and the steered signal becomes

$$\hat{S}(x_i,n)=\frac{\sum_{\ell=1}^{M-L+1}\mathbf{w}^{\mathrm{H}}(x_i,n)\overline{\mathbf{S}}_\ell(x_i,n)}{M-L+1}, \tag{15}$$

which gives more weight to the central elements and causes a tapering of the full length aperture and reduces the lateral resolution. Because the MV beamformer is sensitive to steering errors, the optimization in (11) can be modified to require that

$$\begin{aligned}\mathbf{w}[n]^{\mathrm{H}}(\mathbf{a}[n]+\mathbf{d}[n])&=1\\ \|\mathbf{d}\|_2^2&\le\varepsilon^2.\end{aligned} \tag{16}$$

This means that the covariance matrix, $\hat{\mathbf{R}}(x_i,n)$ is replaced by $\hat{\mathbf{R}}(x_i,n)+\varepsilon\mathbf{I}$ in (12), where $\mathbf{I}$ is the identity matrix, the same size as $\hat{\mathbf{R}}(x_i,n)$. We took ε, as suggested in [16] and [17], to be proportional to the power of the observations,

$$\varepsilon=\Delta\cdot\mathrm{tr}\{\hat{\mathbf{R}}(x_i,n)\}, \tag{17}$$

where $\mathrm{tr}\{\cdot\}$ is the trace operator and Δ is usually a small gain on the order of $1/100L$.

Because we apply the MV beamforming with STB, we note that $\{\overline{\mathbf{S}}_\ell(x_i,n)\}$ are not available and must be generated using (1). Namely, its entries are given by

$$\tilde{S}_m(x_i,n-\tau_\ell(x_i))=\sum_b h(x_i,b)S_m(x_b,n-\tau_\ell(x_i)). \tag{18}$$

This means that before applying the estimation and weighting schemes for the MV beamforming as detailed previously, the signals along Rx scan lines (identified by x_i) should be interpolated from adjacent measured signals along beams b of a certain interpolation order.

III. Methods

As mentioned earlier, we have conducted extensive experiments using simulated data, real phantom data, and real cardiac data. In the following, we describe in some detail the setup and information pertaining to these experiments. In all our experiments, we have applied SLA and 4MLA. For the use of STB compensation we have, for each transmitted beam b, 8 receive beams enumerated as $i=4b+\ell$, $\ell\in\{\pm1,\pm2,\pm3,\pm4\}$ four of which are common to two consecutive transmit beams. The interpolation filter we used is then given by

$$[h(x_i,b),h(x_i,b+1)]=\begin{cases}[0.875 & 0.175] & \text{for } i=4b+1\\ [0.675 & 0.425] & \text{for } i=4b+2\\ [0.425 & 0.675] & \text{for } i=4b+3\\ [0.175 & 0.875] & \text{for } i=4b+4.\end{cases} \tag{19}$$

A. Simulation Setup and Selecting Aperture Width

For our experiment with simulated data we used a setup similar to the one used in the experiments described in [10] for 4MLA.

Namely, an 18.5-mm aperture with 96 elements was used, and a Gaussian pulse at the central frequency of 3.5 MHz and 85% fractional bandwidth was simulated. The transmission was focused at 70 mm depth and no apodization was applied on transmission. The returned signals were sampled using 20 MHz sampling frequency. The IQ envelope of the signal was extracted and sampled using linear interpolation at the appropriate dynamic delays. Three options were applied with dynamic receive beamforming: No apodization (rectangular window), Hamming apodization, and MV adaptive apodization.

A 20° sector was spanned with 32 Tx lines in SLA mode and 8 Tx lines in 4MLA mode. The number of Rx lines was the same in both cases, 32 lines with 0.625° line density.

An important point to consider when simulating the MLA setting is the transmission beam pattern. To achieve efficient lateral coverage in MLA mode, a wider beam pattern is needed, as described in [3]. It is even more important when using STB compensation, because the transmission width should span at least twice the lateral spacing of uncompensated MLA to uphold the Nyquist criterion. In [10], the authors have used 0.25 of the aperture to generate a wider beam. We have analyzed the beam profiles for this setting and show that this generates a beam wider than necessary to hold the Nyquist criterion in [3], and we instead used 0.5 of the active aperture. Although using a wide profile on transmit helps to reduce MLA-induced artifacts, it also causes a poorer lateral resolution in the process; hence, using a larger aperture helps preserve lateral resolution.

We have compared the Tx profiles for the 0.25 and 0.5 apertures. Using a wider aperture narrows the beam profile as known through the relation

$$D_F=\frac{F}{a}\lambda, \tag{20}$$

where a is the aperture length, F is the depth distance to the focal spot, and D_F is the profile width at the focus.

Fig. 1 shows the Tx pressure fields at the focal depth of 70 mm for 0.25 and 0.5 active apertures at the central steering angle of 0°. It is important to note that the transition region from near field to far field for 0.25 active aperture with a width of 4.625 mm is $R_C = a^2/\lambda = a^2 f_c/c = ((4.625\ \text{mm})^2 \cdot (3.5e^6/\text{s}))/(1540e^3\ \text{mm/s}) = 48.6$ mm, which is smaller than the desired focus of 70 mm. That is why the cross section of the pressure field at 70 mm does not show a single main lobe for 0.25 active aperture. At the same time, the transition region of 0.5 active aperture with a width of 9.25 mm is $R_C = 194.5$ mm, which is larger than the 70 mm depth, and hence the 70 mm focus is possible and the pressure field has a clear main lobe. When looking at the magnified profiles (see same figure) it is clearly observed that 0.5 active aperture can be used to span 4 adjacent Rx lines with pressure no less than −3 dB, and 0.25 active aperture spans 8 adjacent Rx lines approximately above −3 dB which is needed for linear interpolation with STB, meaning that the Tx profile for 0.25 active aperture is approximately twice as wide above −3 dB than that of 0.5 active aperture, as expected. Using these results, we have used 0.5 active aperture for MLA simulations without STB, and 0.25 active aperture for STB-compensated MLA simulations, which is needed to maintain the Nyquist criterion for angular sampling so that the Rx data can be interpolated from adjacent transmissions.

B. Experimental Data Setup

For the experimental data analysis, we have used a GE experimental breadboard ultrasound system, courtesy of GE Healthcare, Israel. The system was applied to an acrylic phantom and a healthy heart of a human subject. The same transducer was used for both trials, but with different line density and receive settings.

An 18.56-mm probe with 64 elements was used. Its central frequency was 2.5 MHz, and it transmitted 1.5 periods of Gaussian pulse at 1.71 MHz frequency with 60% bandwidth. On receive, the second harmonic of 3.42 MHz was used for beamforming. Tx focus was 14 cm. The RF signals for each channel were sampled at 20 MHz. Afterward, the signals were re-sampled according to the calculated delays for dynamic receive using linear interpolation, their in-phase and quadrature (IQ) components were extracted using the Hilbert function, and the appropriate apodization was applied according to the selected method. The delays, quadrature extraction, and apodizations were implemented separately using Matlab (The MathWorks Inc., Natick, MA). The FOV of the scan covered 75° with 76 lines, which gave a 1.013° line density. The maximum depth was 16 cm.

For the cardiac data, the probe, its transmitted pulse, and Tx focus were the same as those used for scanning the phantom. The RF signals for each channel were sampled at 50 MHz frequency, and then were demodulated, shifting them 3.42 MHz. The resulting signals were re-sampled at 4 MHz frequency and their IQ components were extracted. Afterward, the IQ signals were re-sampled according to the calculated delays for dynamic receive using linear interpolation, and the appropriate apodization was applied according to the selected method. The delays and apodizations were implemented separately using Matlab. The FOV of the scan covered 75° with 120 lines, which gave a 0.625° line density. The maximum depth was 16 cm.

For this part of the analysis, we chose to compare the MV beamformer images to DAS with rectangular window only, because this is a commonly used window for comparison; it preserves resolution at the expense of contrast compared with windows with tapering at the edges of the aperture, such as Hamming or Hanning windows.

C. Simulating a Wider Transmit Pulse for Experimental Data

The RF data for the phantom and the cardiac IQ data were both obtained using standard SLA mode, where the transmitted pulse spans a single receive line laterally, as this is what the system allowed at the time. We had to simulate a wider transmit pulse from this data. To simu-

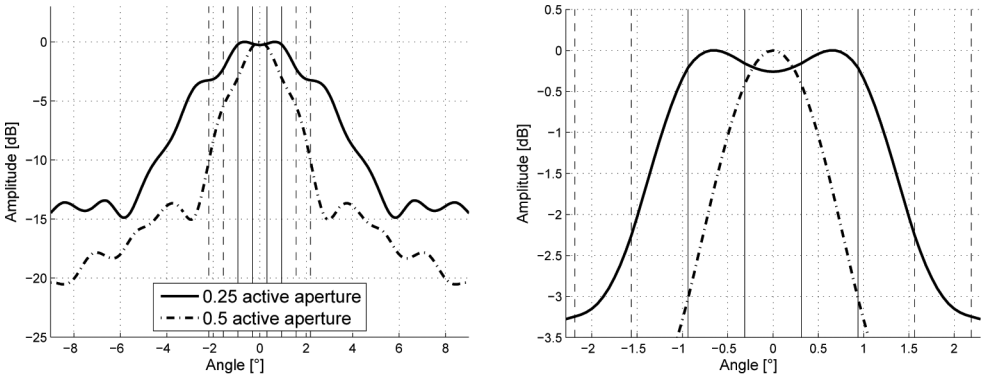

Fig. 1. Tx pressure fields at 0° steering angle and 70 mm depth focus used for the simulation. Solid lines represent the locations of the adjacent Rx lines in the same MLA group, dashed lines represent the Rx lines also used in STB. (a) Comparison of the Tx profiles at the focal depth. (b) Magnification of the region spanned by 8 Rx lines used in STB mode.

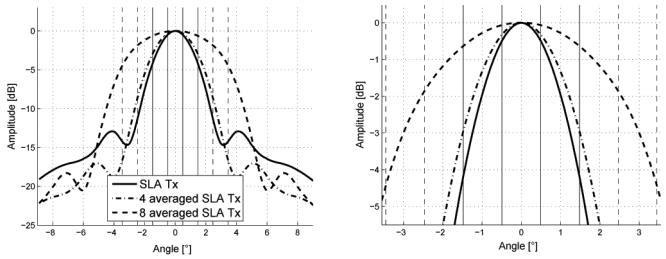

Fig. 2. Simulated Tx pressure fields at 0° steering angle and 140 mm depth focus used for MLA pulse simulation of real data. Solid lines represent the locations of the adjacent Rx lines in the same MLA group, dashed lines represent the Rx lines also used in STB. (a) Comparison of the Tx profiles at the focal depth. (b) Magnification of the region spanned by 8 Rx lines used in STB mode.

late an MLA scan setting, the received signals of adjacent scan lines were averaged. For an uncompensated 4MLA setting, the signals from groups of 4 adjacent SLA scan lines were averaged for each element. For the STB-compensated setting, the signals from groups of 8 adjacent SLA scan lines were averaged with overlaps of 4 lines, which would be expected of an overlapping wide transmission for STB acquisition. Fig. 2 shows the pressure fields' cross sections at the focal depth of 14 cm, and magnified view on the region of 8 adjacent Rx lines.

It can be seen that to get proper lateral coverage for STB, the data from 8 adjacent scan lines should be averaged, because the profile in the region spanning 8 scan lines is in the range of −4 dB, whereas if averaging only 4 lines, the furthest lines have −15 dB amplitude compared with the peak at the center of transmission, which may incur aliasing for 2-way profiles unless the Rx profile is wide enough to compensate for it. It is sufficient to average 4 adjacent scan lines when non-compensated MLA is used, because then it needs to span only 4 Rx lines.

It is important to note that in a real scenario, the actual Tx profile would be wider, which will reduce SNR. In the observed results in subsections IV-B and IV-c, the SNR is improved as a result of the use of the simulated wide Tx profile, which is narrower than real Tx profile in 4MLA beamforming.

IV. Results and Discussion

As mentioned earlier, we have used Field II simulations as well as experimental data of a phantom and heart. We will show that both the simulations and real data experimental results support our claim that combining the STB with the MV gives superior performance to either separately used MLA setting.

A. Simulated Phantom Results

We have investigated the effects of MLA in an environment similar to the heart, where strong reflections in the heart wall are adjacent to weak reflections of blood inside the chamber, and intermediate reflections of tissue outside the heart. For that purpose, we have simulated an elliptic ring centered along the main axis, at 0°, at a depth of 69 mm. The outer perimeter of the ring is defined by an ellipse with main axis lengths 7 and 11 mm, such that $x^2/7^2 + z^2/11^2 = 1$. The inner perimeter of the ring is defined by an ellipse with main axes 5 and 9 mm, such that $x^2/5^2 + z^2/9^2 = 1$. The ring is cylindrical, and has the same shape for all pitch (y) values.

The imaged region spanned from −9 to 9 mm in azimuth (x), −5 to 5 mm in pitch, and 56 to 84 mm in depth (z). The density of all scatterers inside the chamber, in the ring, and outside the ring was set to be 10 scatterers per resolution cell of size λ^3, where $\lambda = c/f_c$ is the central wavelength that matches the central frequency, f_c, as suggested in [23]. The difference in reflectance was according to the standard deviation (STD) of the Gaussian drawn amplitudes inside the different regions. The mean values of the Gaussian was 0 for all regions. Outside the ring, its STD was set to 1, inside the inner ellipse to 0.1, and inside the ring to 10. Between the ring and the inner ellipse (chamber) there was a difference of 2 orders of magnitude (in terms of STD).

In addition, 2 pairs of strong reflectors were simulated deeper than the ring for lateral resolution measurements. The azimuthal distance between the reflectors was 3 mm. The first pair was at a depth of 81 mm and the second at the depth of 83 mm. The fixed amplitude of the strong reflectors was set to 500.

The simulated chamber was processed using standard SLA DAS beamforming with rectangular and Hamming windows and MV beamforming. In addition, it was processed using 4MLA setting without and with STB compensation. In both cases, 0.5 of the aperture was active in transmit. The MV beamforming was done using a subarray of length $L = 48$ (half of the aperture), $\Delta = 1/100L$, and $K = 5$ (11 samples, which corresponds to 0.42 mm and 0.96 wavelengths).

Fig. 3 shows a comparison of the results for the 3 beamformers using SLA and STB-compensated and uncompensated 4MLA. The images have a display range of 60 dB. Below each image, there is a plot of the C_c values, which represent the correlation of adjacent scan lines as defined in (7). Grey bars represent the correlation between Rx lines in the same MLA group; black lines represent the correlation between Rx lines of different MLA groups. The whole displayed depth was used for correlation measurements. Notice the sharp transition seen inside the chamber between the brighter reflections and the darker, weak reflections, when no STB compensation is applied. This artifact stems from the side lobes of the ring projected laterally into the chamber. Without STB compensation this sharp transition is caused by the skewing and warping effects of MLA. This is noticeable even with MV beamforming which potentially can reduce interference for the ring's side lobes; because they are too strong, it is manifested inside the chamber as seen by the straight lines following the transitions between adjacent MLA groups centered inside

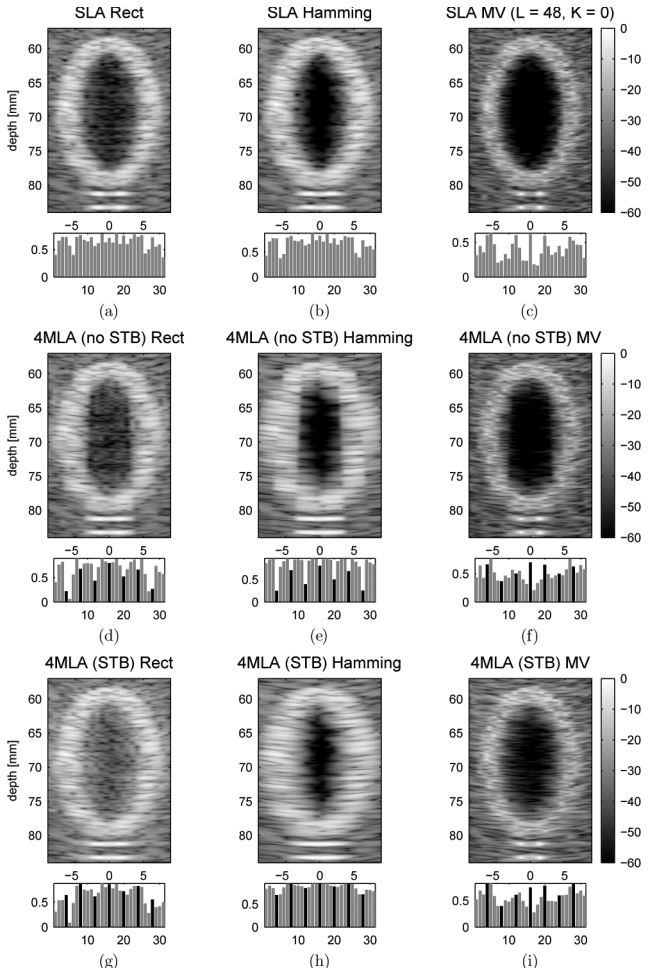

Fig. 3. Simulated ventricle. (a) DAS rectangular window SLA, (b) DAS Hamming window SLA, (c) MV SLA (L = 48, K = 5), (d) Rect 4MLA (uncompensated), (e) Hamming 4MLA (uncompensated), (f) MV 4MLA (uncompensated), (g) Rect 4MLA STB, (h) Hamming 4MLA STB, (i) MV 4MLA STB. Corresponding C_c values of adjacent Rx lines are below each image.

the ring and the chamber accordingly. STB compensation reduces this phenomenon, creating a gradual transition between the ring and the chamber. This is true for all three methods of beamforming, and especially relevant for the Hamming window, which has a wide Rx profile that emphasizes the MLA artifacts. Notice also the well-defined shape and edges of the ring using STB-compensated MV beamforming compared with SLA rectangular DAS.

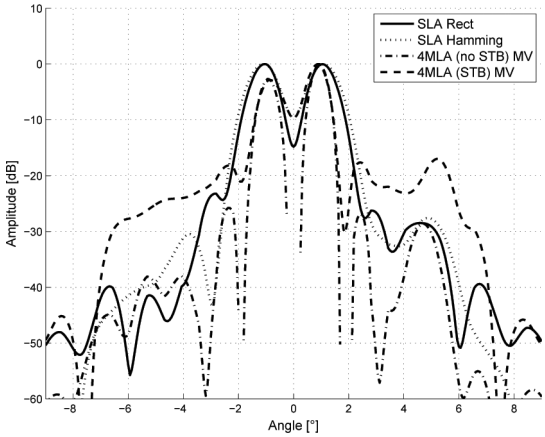

Fig. 4. Steered responses of target points for DAS (rectangular and Hamming windows) and 4MLA with MV (with and without STB compensation).

It can be observed that the C_c values are lower for transition between MLA groups than inside the MLA groups for the uncompensated MLA case. Using STB brings them to approximately the same level. This is most noticeable for Hamming window and less noticeable for MV beamforming, where the transition artifact is subtle and can be seen only in transitions between strong and weak reflections between MLA groups.

Fig. 4 shows a steered response through the strong reflectors at 81 mm depth. Note the narrower main lobe width for the strong reflectors when using MV with 4MLA compared with the main lobe width of rectangular window SLA. In addition, notice the lower side lobes the MV beamformer has compared with SLA rectangular DAS.

We have measured the main lobe width at −3 dB level and side lobe maximum levels of the strong reflectors. The results are given in Table I. From these measurements, it can be seen that MV has narrower main lobes, and hence improved lateral resolution with non-compensated MLA over that of SLA DAS. In addition, MV's side lobes without STB compensation are lower than SLA DAS. It is also important to notice that applying STB in 4MLA mode increased the width of the main lobe and the side lobes levels for all three beamformers over those of their SLA counterparts because of the wide Tx beam profile needed to span two adjacent MLA groups in STB-compensated mode.

TABLE I. Main Lobe Width and Side Lobe Levels for Point Reflectors.

SLA/MLA	Beamforming	Main lobe width [°]	Max side lobes level [dB]
SLA	DAS rect	0.87	−23.2
	DAS Hamming	1.00	−27.6
	MV	0.55	−24.6
MLA no STB	DAS rect	1.12	−26.5
	DAS Hamming	1.70	−27.7
	MV	0.57	−25.8
MLA with STB	DAS rect	2.00	−16.9
	DAS Hamming	3.44	−20.2
	MV	1.69	−17.6

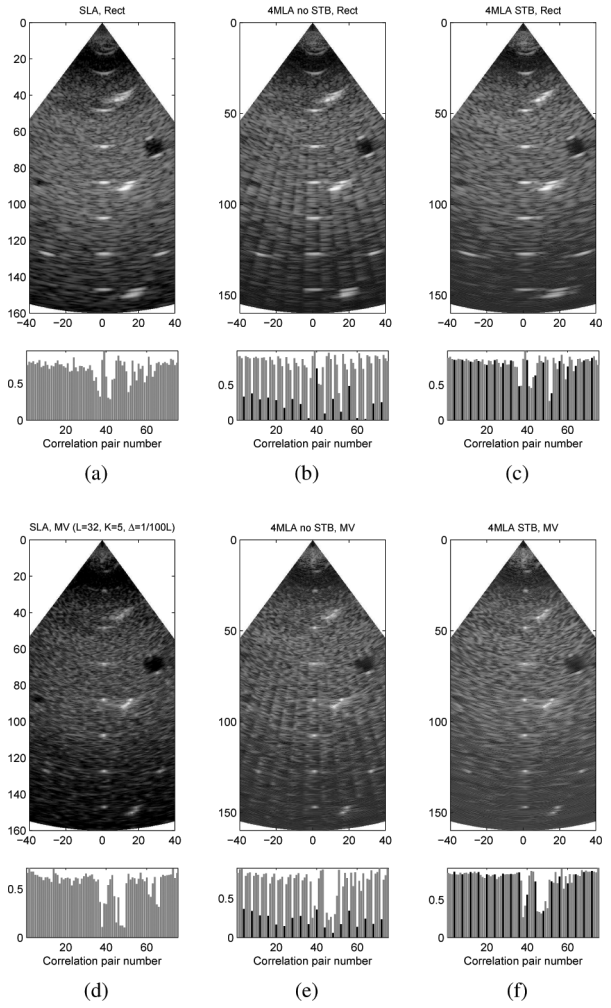

Fig. 5. Phantom images with rectangular apodization (DAS) and MV beamformer: (a) DAS-SLA (76 lines), (b) DAS–non-compensated 4MLA (19 lines) from averaged 4 scan lines, (c) DAS–STB-compensated 4MLA from 8 averaged scan lines, (d) MV-SLA, (e) MV–Non-compensated 4MLA, (f) MV–STB-compensated 4MLA.

The simulations results show that one can achieve better separation and lateral resolution using MV beamforming in an uncompensated MLA setting than SLA DAS. In addition to that, a method such as STB is needed to compensate for MLA-induced artifacts of block-like sharp transitions between adjacent MLA groups in strong reflecting media next to weak reflecting media.

B. Phantom Analysis

An acrylic phantom (405GSX LE, Gammex Inc., Middleton, WI) was used in the first part of the trials for assessment of lateral resolution improvement. It contained needle point reflectors embedded in an acrylic medium, as well as small lesion-mimicking inclusions.

Fig. 5 shows 6 images with DAS rectangular window and MV beamformer, comparing SLA, non-compensated 4MLA and STB-compensated approaches. MV beamforming was applied using the parameters $L = 32$, $K = 5$ (11 temporal samples, 0.42 mm, 0.96 wavelengths for the second harmonic), and $\Delta = 1/100L$. The images have a display range of 60 dB. Below each image is a correlation plot of its adjacent Rx lines measured from 32 to 160 mm depth. The block-like artifacts in the transition between MLA groups are clearly seen without STB compensation. With STB compensation, the artifacts are clearly reduced. This phenomenon can also be seen in the correlation patterns of adjacent Rx lines. The black bars in the correlation plots represent the correlation between Rx lines of different MLA groups. Without STB compensation, the correlation is lower than the correlation of Rx lines in the same MLA group.

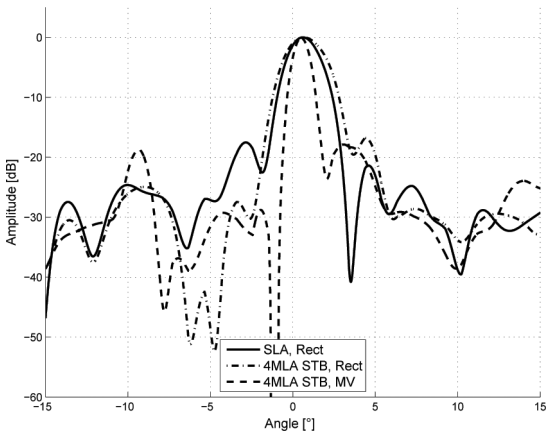

Fig. 6. Steered responses of wire target at 88 mm depth for rectangular window DAS SLA and STB-compensated 4MLA generated with rectangular DAS and MV beamformers.

As opposed to the Field II simulations, in which no significant transition artifacts were observed for non-compensated MLA with MV beamforming, Fig. 5(e) shows clear straight lines in the transition between adjacent MLA groups. This phenomenon can be also observed in the sharp correlation drop between Rx lines from adjacent MLA groups, as demonstrated by the black bars, which are much lower than the gray bars (we recall again that the gray bars represent the correlation within MLA groups). As expected, STB compensation removes these transition artifacts.

Overall, the wire targets have a much sharper appearance with MV beamforming compared with SLA DAS, even with a much wider Tx profile than the narrow Tx profile used for SLA DAS. The cyst's shape is less obscured by the strong reflectors above and below it with the MV beamformer than the DAS images.

Fig. 6 displays the steered responses around a wire target at 88 mm depth for DAS SLA without STB, and DAS and MV with STB-compensated 4MLA. We observe a slight deterioration of lateral resolution when SLA and STB-compensated MLA are compared. However, by comparing the main lobes, we see a significant resolution enhancement when MV is applied to the STB-compensated MLA, outperforming even the SLA. This is especially impressive as we recall that in the STB-compensated MLA case the Tx beam is much wider.

TABLE II. PHANTOM DATA MAIN LOBE WIDTH AND D_C VALUES FOR RECTANGULAR DAS AND MV BEAMFORMERS.

SLA/MLA	Beamforming	Main lobe (−3 dB) [°]	D_c [%]
SLA	DAS rect	1.86	1.8
	MV	1.08	−2.3
MLA no STB	DAS rect	2.39	69.3
	MV	1.09	68.8
MLA with STB	DAS rect	2.43	3.7
	MV	1.03	−1.9

Table II summarizes the comparison of lateral resolution and D_c values for the phantom. The D_c value is a measurement for the overall relative decorrelation (0 to 100%) that exists in the image as described in (8). It is interesting to note that the main lobe for DAS is wider when applying STB, because it requires a wider Tx profile, whereas the main lobe for MV is narrower after applying STB. It is even narrower than the main lobe width of SLA with MV beamforming. This can be explained by the fact that the wire target lies in the transition between the MLA groups, and thus it is slightly suppressed by the Tx profiles of the adjacent transmission. When the targets lie in the center of the MLA group, as in the simulation results in subsection IV-A, the main lobe will be wider because of the wider Tx beam profile applied in STB-compensated MLA beamforming.

Looking at the D_c values, the improvement in terms of scan line correlation is seen with STB compensation. There is a sharp drop in D_c value for DAS after STB compensation compared with non-compensated MLA. It is also noticeable for the MV beamformer, as the D_c value of 68.8 shows a very high decorrelation between MLA groups. STB compensation brings the D_c value to the same level as SLA MV.

C. Cardiac Data Analysis

In the second part of the trials with real data, a healthy heart of a human subject was imaged. The chosen frame shows a cross section of the left ventricle. Fig. 7 shows 6 images with DAS rectangular window and MV beamformer comparing SLA, non-compensated 4MLA, and STB-compensated 4MLA. MV beamforming was applied using the parameters $L = 32$, $K = 1$ (3 temporal samples, 0.58 mm, 1.28 wavelengths for the second harmonic), and $\Delta = 1/100L$. The images have a display range of 60 dB.

As can be seen from the images, there are strong reflections in the heart muscle next to weakly reflecting tissue and almost non-reflecting blood inside the ventricle and chamber. This causes sharp lines between MLA groups to appear in the transition between the different media. The strong reflectors are smeared across the MLA group where they appear, whereas the MLA groups next to them are affected mainly by the low reflections. This property of the scanned medium enhances the MLA induced artifacts, beecause now the data that is summed by the asymmetric profiles that tend toward the center of the MLA groups dominates the whole lateral range spanned by the MLA group.

When comparing the MV images to DAS, an improvement in lateral resolution can be seen in the form of sharper speckle appearance, although there is no contrast improvement, and it even seems that there is a loss of contrast relative to DAS. This stems from the fact that the strong reflections in the heart wall have a smaller lateral signature with MV beamforming, whereas some speckles in the blood are more emphasized by the MV beamformer relative to DAS because of the interference cancellations.

Table III shows the overall decorrelation D_c values for the images in Fig. 7. The results for MV clearly show that the decorrelation rise when using non-compensated MLA compared with SLA, and approximately the same correlation as SLA with STB-compensated MLA.

V. CONCLUSIONS

In this work, we have shown that an MV beamformer in a non-compensated MLA setting may have sharp transition artifacts, similar to those seen in MLA setting with fixed apodization beamforming. To our best knowledge, this phenomenon of the MV beamformer was not encountered in the literature before and was not anticipated, because the MV beamformer outperforms fixed apodization beamformers in many cases in terms of image quality. Using MV beamforming with STB compensation generated artifact-free images.

The scenario that emphasized these artifacts most was that of strong reflections next to a weakly reflecting medium, such as the one that can be seen in the heart wall

TABLE III. CARDIAC DATA D_C VALUES FOR RECTANGULAR DAS AND MV BEAMFORMERS.

SLA/MLA	Beamforming	D_c [%]
SLA	DAS rect	0.7
	MV	1.0
MLA no STB	DAS rect	42.8
	MV	41.7
MLA with STB	DAS rect	1.3
	MV	1.1

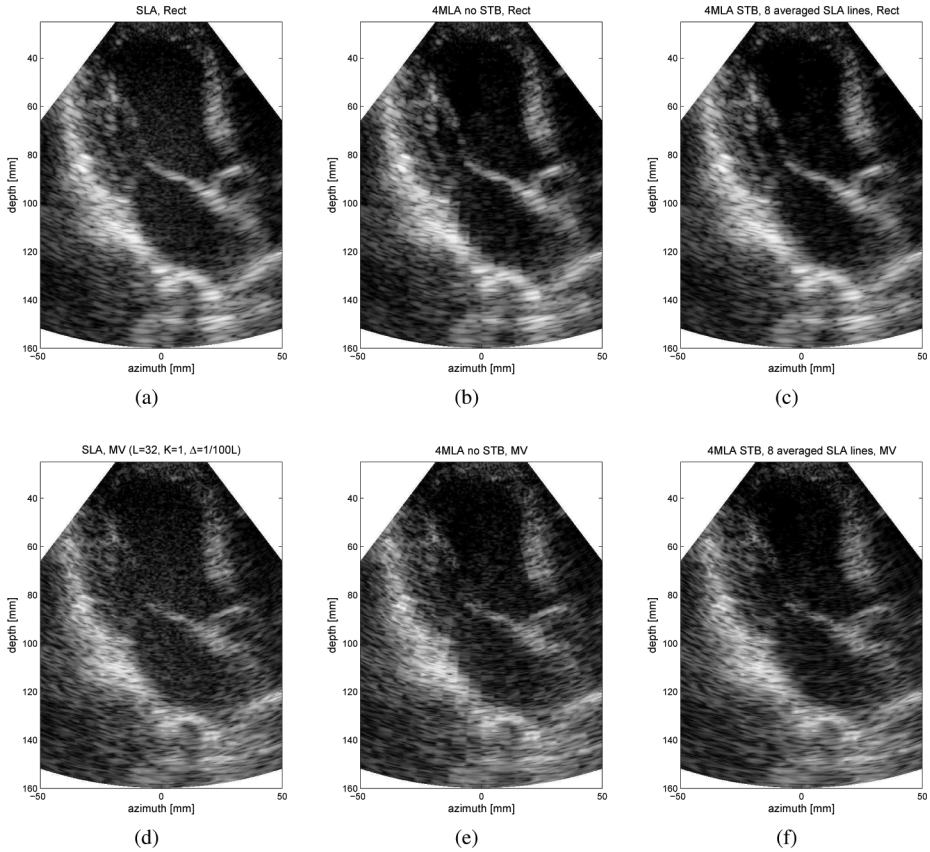

Fig. 7. Cardiac images with rectangular apodization (DAS) and MV beamformer: (a) DAS-SLA (120 lines), (b) DAS–non-compensated 4MLA (30 lines), (c) DAS–STB-compensated 4MLA, (d) MV-SLA (d) MV–non-compensated 4MLA, (f) MV–STB-compensated 4MLA.

next to blood-filled chamber. It is vitally important to apply some sort of MLA compensation to reduce these artifacts in a clinical setting, even with a data-dependent beamforming such as the MV beamformer, because it cannot eliminate these artifacts on its own. On the other hand, we have also demonstrated that STB compensation in the MLA setting comes at the cost of resolution and contrast loss.

In conclusion, we have shown that the MV beamformer with STB compensation can produce better results than the MV beamformer without STB compensation, better than those of the STB-compensated DAS beamformer, and even better than those of SLA DAS in terms of lateral resolution in experimental settings.

Acknowledgments

The authors thank GE Healthcare, Israel for access to their experimental ultrasound system.

References

[1] D. P. Shattuck, M. D. Weinshenker, S. W. Smith, and O. T. von Ramm, "Explososcan: A parallel processing technique for high speed ultrasound imaging with linear phased arrays," *J. Acoust. Soc. Am.*, vol. 75, no. 4, pp. 1273–1282, 1984.

[2] O. von Ramm, S. Smith, and J. Pavy, "High-speed ultrasound volumetric imaging system. II. Parallel processing and image display," *IEEE Trans. Ultrason. Ferroelectr. Freq. Control*, vol. 38, no. 2, pp. 109–115, Mar. 1991.

[3] T. Hergum, T. Bjastad, K. Kristoffersen, and H. Torp, "Parallel beamforming using synthetic transmit beams," *IEEE Trans. Ultrason. Ferroelectr. Freq. Control*, vol. 54, no. 2, pp. 271–280, 2007.

[4] L. J. Augustine, "High resolution multiline ultrasonic beamformer," U.S. Patent 4 644 795, Feb. 24, 1987.

[5] K. E. Thiele and A. Brauch, "Method and apparatus for dynamically steering ultrasonic phased arrays," U.S. Patent 5 322 068, Jun. 21, 1994.

[6] T. J. Hunt, B. M. Herrick, K. K. Robertson, K. E. Thiele, and M. J. Ziel, "Ultrasound imaging system using line splicing and parallel receive beam formation," U.S. Patent 5 462 057, Oct. 31, 1995.

[7] G. L. Holley and I. M. Guracar, "Ultrasound multi-beam distortion correction system and method," U.S. Patent 5 779 640, Jul. 14, 1998.

[8] D.-l. D. Liu, J. C. Lazenby, Z. Banjanin, and B. A. Mcdermott, "System and method for reduction of parallel beamforming artifacts," U.S. Patent 6 447 452, Sep. 10, 2002.

[9] N. J. Wright, S. H. Maslak, D. J. Finger, and A. Gee, "Method and apparatus for coherent image formation," U.S. Patent 5 623 928, Aug. 11, 1997.

[10] J.-F. Synnevag, A. Austeng, and S. Holm, "Benefits of minimum-variance beamforming in medical ultrasound imaging," *IEEE Trans. Ultrason. Ferroelectr. Freq. Control*, vol. 56, no. 9, pp. 1868–1879, Sep. 2009.

[11] J. Capon, "High-resolution frequency-wavenumber spectrum analysis," *Proc. IEEE*, vol. 57, no. 8, pp. 1408–1418, Aug. 1969.

[12] J. A. Jensen, "Field: A program for simulating ultrasound systems," *Med. Biol. Eng. Comput.*, vol. 34, suppl. 1, pt. 1, pp. 351–353, 1996.

[13] T. Bjastad, S. Aase, and H. Torp, "The impact of aberration on high frame rate cardiac B-mode imaging," *IEEE Trans. Ultrason. Ferroelectr. Freq. Control*, vol. 54, no. 1, pp. 32–41, Jan. 2007.

[14] J. Mann and W. Walker, "A constrained adaptive beamformer for medical ultrasound: Initial results," in *Proc. IEEE Ultrasonics Symp.*, 2002. vol. 2, pp. 1807–1810.

[15] M. Sasso and C. Cohen-Bacrie, "Medical ultrasound imaging using the fully adaptive beamformer," in *Proc. IEEE Int. Conf. Acoustics, Speech, and Signal Processing*, 2005, vol. 2, pp. 489–492.
[16] J. Synnevag, A. Austeng, and S. Holm, "Minimum variance adaptive beamforming applied to medical ultrasound imaging," in *IEEE Ultrasonics Symp.*, 2005, vol. 2, pp. 1199–1202.
[17] J.-F. Synnevag, A. Austeng, and S. Holm, "Adaptive beamforming applied to medical ultrasound imaging," *IEEE Trans. Ultrason. Ferroelectr. Freq. Control*, vol. 54, no. 8, pp. 1606–1613, Aug. 2007.
[18] F. Vignon and M. Burcher, "Capon beamforming in medical ultrasound imaging with focused beams," *IEEE Trans. Ultrason. Ferroelectr. Freq. Control*, vol. 55, no. 3, pp. 619–628, Mar. 2008.
[19] Z. Wang, J. Li, and R. Wu, "Time-delay- and time-reversal-based robust capon beamformers for ultrasound imaging," *IEEE Trans. Med. Imaging*, vol. 24, no. 10, pp. 1308–1322, Oct. 2005.
[20] J. Evans, J. Johnson, and D. Sun, "High resolution angular spectrum estimation techniques for terrain scattering analysis and angle of arrival estimation," in *Proc. 1st ASSP Workshop Spectral Estimation*, 1981, vol. 1, p. 1.
[21] T.-J. Shan, M. Wax, and T. Kailath, "On spatial smoothing for direction-of-arrival estimation of coherent signals," *IEEE Trans. Acoust. Speech Signal Process.*, vol. 33, no. 4, pp. 806–811, Aug. 1985.
[22] J.-F. Synnevag, C.-I. Nilsen, and S. Holm, "Speckle statistics in adaptive beamforming," in *Proc. IEEE Ultrasonics Symp.*, 2007, pp. 1545–1548.
[23] R. Wagner, M. Insana, and S. Smith, "Fundamental correlation lengths of coherent speckle in medical ultrasonic images," *Ultrasonics, Ferroelectrics and Frequency Control, IEEE Transactions on*, vol. 35, no. 1, pp. 34–44, jan. 1988.

Adi Rabinovich received his B.Sc. degree from the Biomedical Engineering faculty at the Technion-Israel Institute of Technology, Haifa, Israel in 2010. From 2011 to 2013, he was with MedicVision, Haifa, Israel, where he was working on the development and improvement of computed tomography imaging algorithms. He is currently pursuing an M.Sc. degree in electrical engineering at the Technion, and working as a senior developer at ImageGalil, Haifa, Israel, on ultrasound imaging quality and performance improvement. His research interests include medical signal and image processing, computer vision in medical imaging, and fast implementations of medical imaging algorithms.

Zvi Friedman received the B.Sc. degree in physics from the Technion-Israel Institute of Technology, Haifa, in 1966, the M.Sc. degree from the Weizmann Institute of Science, Rehovot, in 1970, and the Ph.D. degree in solid-state physics from the Tel Aviv University, Israel, in 1974. He joined the ultrasound division of Elscint, Haifa, as a Senior Scientist in 1991. Since 1998, this division became part of the cardiovascular activity in GE Healthcare. His main areas of interest include application of advanced signal processing methods to ultrasonic imaging in general and to beamforming in particular. He is also working on the development of advanced cardiac applications.

Arie Feuer received the B.Sc. and M.Sc. degrees in mechanical engineering at the Technion-Israel Institute of Technology, Haifa, Israel, in 1967 and 1973, respectively, and the Ph.D. degree from Yale University in CT in 1978. From 1967 to 1970, he was with Technomatics Inc., working on the design of automatic machines. From 1978 through 1983, he worked for Bell Labs in network performance evaluation. In 1983, he joined the faculty of Electrical Engineering at the Technion, where he is currently a professor emeritus. Professor Feuer is a Fellow of the IEEE. His current research interests include medical ultrasound imaging, resolution enhancement of digital images and videos, sampling and combined representations of signals and images, and adaptive systems in signal processing and control.